Supplemental Information for "Bedrock River Erosion through Layered Rocks: Quantifying Erodibility through Kinematic Wave Speed"

Nate A. Mitchell[1] and Brian J. Yanites[1]

[1]Indiana University, Bloomington, Indiana, USA

Correspondence to: Nate A. Mitchell (natemitc@indiana.edu)

S1: Automated system for measuring contact migration rates

To track the movement of specific contacts in our numerical models, there must be a system for determining if each contact was observed in the last time step evaluated or if it is a new contact. Our approach for this involves assigning each contact a designation (e.g., contact #1, #2, etc.). When our automated system proceeds to the next time step, it then determines if the first contact (contact with the lowest elevation) is the same as the first contact from the last time step. This comparison considers which units are above and below the contact; if the first contact in the previous time step had the weak unit beneath it, but the first contact now has the strong contact beneath it, then this first contact is a new contact (i.e., the first contact from the previous time step has migrated further upstream, and the newly identified contact has only just entered the region where we record contact migration rates). We also use the recorded χ values at each contact. Consider, for example, if the first contact encountered sits over the same rock type as the first contact encountered in the previous time step but the χ value of the newly encountered contact is higher. In that scenario, two new contacts have just entered the region where contact migration is recorded. Note that this approach requires that contacts cannot migrate too fast relative to the time interval over which contacts are tracked (every 25 ka, larger than model timestep dt = 25 a). For example, a contact cannot migrate so fast that it crosses the entire profile over the 25 ka interval.

Because of the change in contact migration direction when contacts dip downstream ($\phi > 0$), the position where χ equals the damping length scale λ (Eq. 12) is not always appropriate place to set the starting position for tracking contact migration. To define an appropriate starting position, we run the simulation for 50 My (so that a dynamic equilibrium is achieved) and find the lowest position where the absolute value of average channel slope exceeds contact dip. Because there are variations in slope within each rock type, we use the average steepness of the profile to find where the average slope exceeds contact dip. We used the average steepness because it will not change significantly over time, once a dynamic equilibrium is achieved. Instead of using the point where average channel slope equals the contact slope as a starting position, however, we advance the starting position further upstream. We made this decision because the exact area where a new unit is exposed varies slightly, which can be problematic for our contact tracking approach. To avoid such complications near the point where new units are exposed, we advance the starting position upstream by the expected χ-distance a reach extending across both the strong unit and a weak unit would span if the dip was zero ($\phi = 0°$). The distance of a reach extending across one rock type $\Delta\chi$ can be solved using the theory developed by Perne et al. (2017):

$$\Delta\chi_S = \frac{H_S}{\left(\frac{E_S}{K_S}\right)^{1/n} {A_0}^{-m/n}} \tag{S1}$$

where $\Delta\chi_S$ is the χ-distance required for a reach spanning the strong unit when $\phi = 0°$. Erosion rate E_S can be solved with Eq. 12. To solve for $\Delta\chi_W$ with Eq. S1, the variables H_S, E_S and K_S would simply have to be changed to H_W, E_W, and K_S. The length scale we use to adjust the starting position is then $\Delta\chi_S + \Delta\chi_W$. This distance was chosen because it varies with simulation input such that it is never too large or small relative to the profile's elevation range (e.g., one fixed distance would not be applicable across the full range of simulations).

Through a process of trial and error, we found that simulations using lower reference weak erodibilities (K_W) require a larger distance between the point where new units are exposed and the starting position for contact tracking. With lower K_W, there is more variability in the locations where new units are exposed. When the starting position for contact tracking is too close to areas where new units are exposed, the variations in erosion rate can cause Eqs. 14 and 15 (Fig. 10) to become less accurate. To avoid such issues, we define the starting position for contact tracking when $\phi > 0°$ as follows:

$$\zeta = \chi_{exposure} + F(\Delta\chi_S + \Delta\chi_W) \qquad \text{(S2)}$$

where ζ is the χ value defining the starting position for contact tracking, $\chi_{exposure}$ is the χ value closest to the point where average channel slope is equal to the contact slope (where new units will likely be exposed), and F is a factor set by the user through trial and error. In simulations with the low, medium, and high K_W, we use F values of one, three, and four, respectively. These F values allowed for accurate estimations of kinematic wave speed using Eqs. 14 and 15 (Fig. 10).

When the contact dip is low enough (or the erodibility values are high enough), however, there will be no inflection point ($\chi_{exposure} = 0$ m) and all contacts will migrate upstream. To address such situations, we evaluate the starting positions described by both λ (Eq. 7) and ζ (Eq. S2) and use whichever starting position is farther upstream.

Supplemental Figures

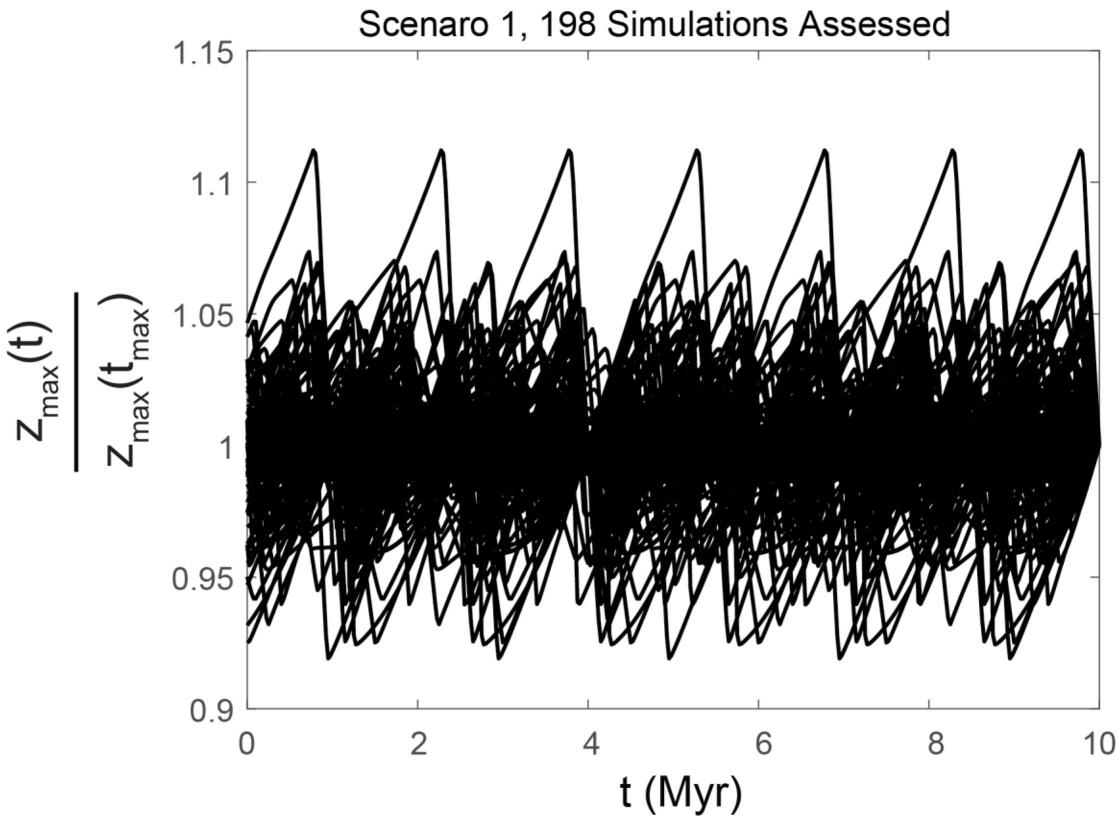

Figure S1. Maximum elevations (z_{max}) over time t normalized by the final maximum elevation ($z_{max}(t_{max})$) for all simulations assessed in scenario 1 (two layers with contact dip $\phi = 0°$; Table 1). Although there are variations in maximum elevation, the range of elevations is constant over time (after the 50 Myr periods of initialization, which are not shown here). These data show that all simulations assessed in scenario 1 had achieved a dynamic equilibrium such that the range of elevations was constant with time. Larger variations in maximum elevation occur for larger contrasts in erodibility.

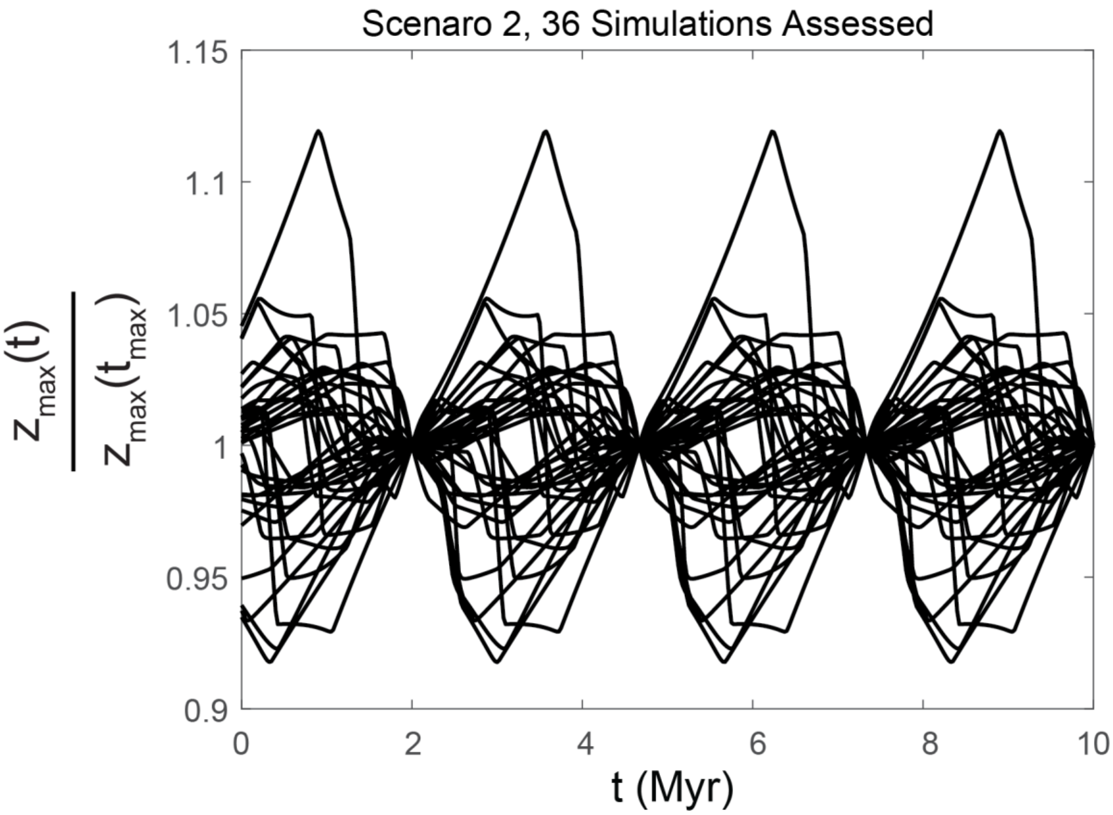

Figure S2. Maximum elevations (z_{max}) over time t normalized by the final maximum elevation ($z_{max}(t_{max})$) for all simulations assessed in scenario 2 (three layers with contact dip ϕ = 0°; Table 1). Although there are variations in maximum elevation, the range of elevations is constant over time (after the 50 Myr periods of initialization, which are not shown here). These data show that all simulations assessed in scenario 2 had achieved a dynamic equilibrium such that the range of elevations was constant with time. Larger variations in maximum elevation occur for larger contrasts in erodibility.

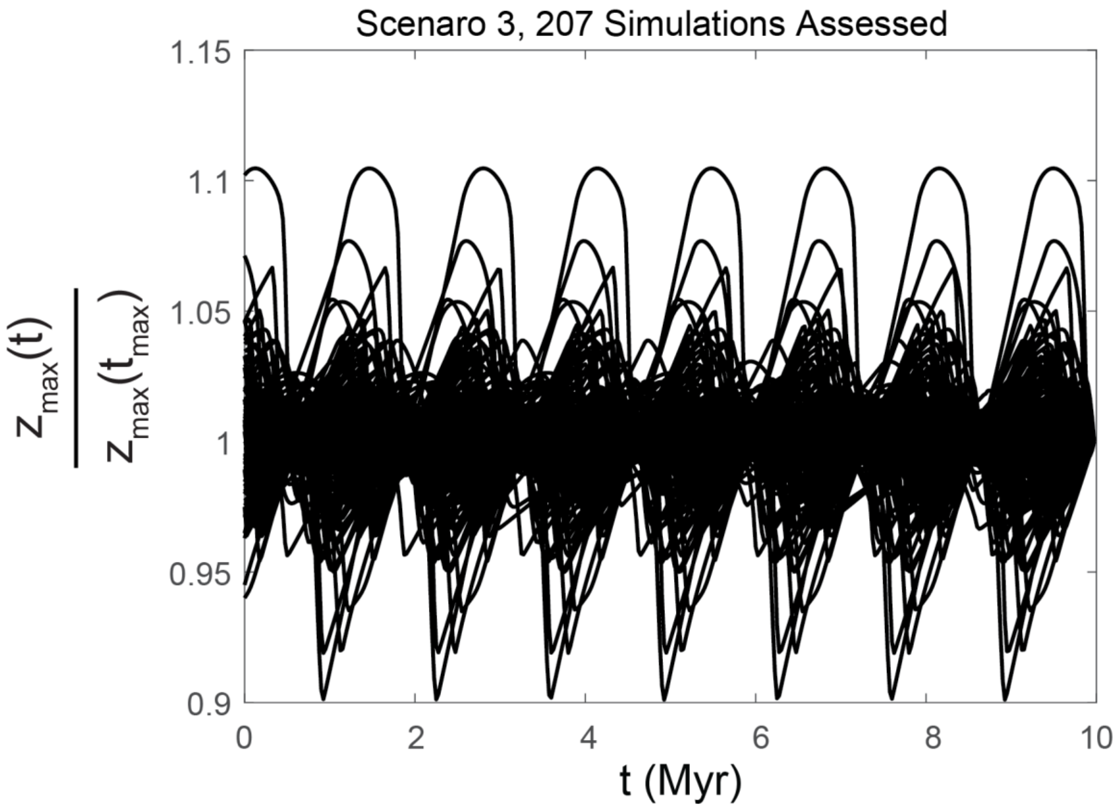

Figure S3. Maximum elevations (z_{max}) over time t normalized by the final maximum elevation ($z_{max}(t_{max})$) for all simulations assessed in scenario 3 (two layers with contact dip $\phi < 0°$; Table 1). Although there are variations in maximum elevation, the range of elevations is constant over time (after the 100 Myr periods of initialization, which are not shown here). These data show that all simulations assessed in scenario 3 had achieved a dynamic equilibrium such that the range of elevations was constant with time. Larger variations in maximum elevation occur for larger contrasts in erodibility.

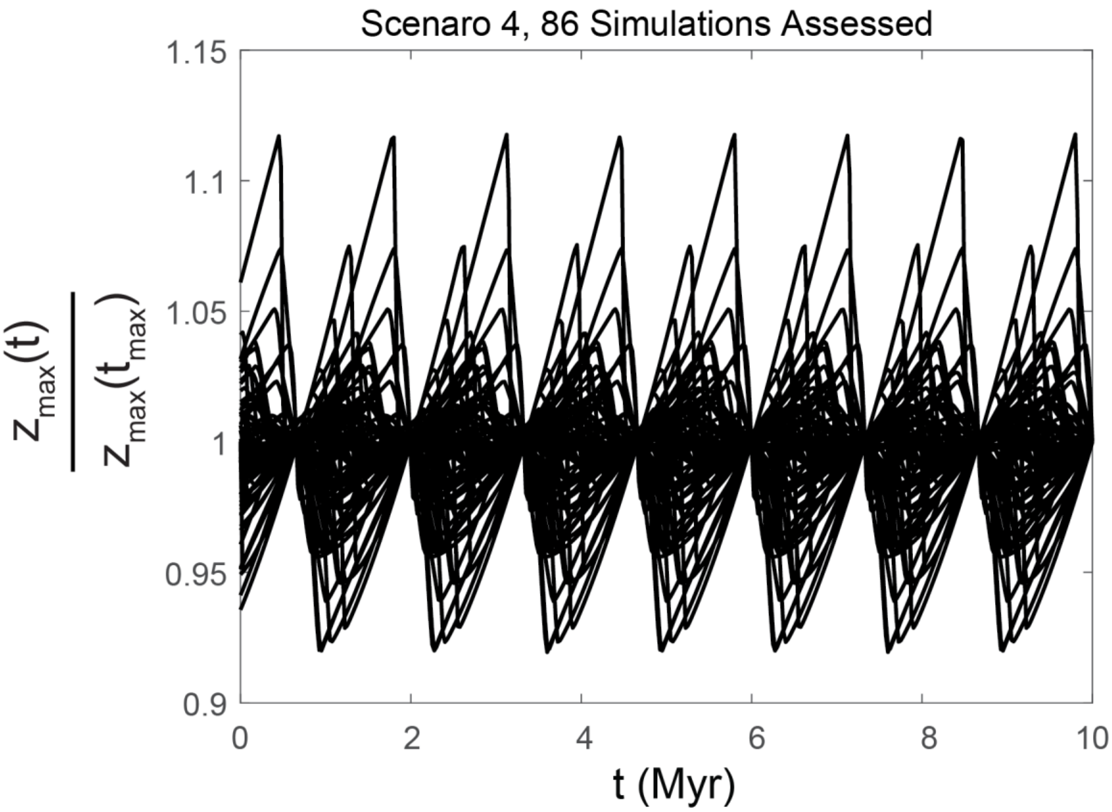

Figure S4. Maximum elevations (z_{max}) over time t normalized by the final maximum elevation ($z_{max}(t_{max})$) for all simulations assessed in scenario 4 (two layers with contact dip $\phi > 0°$; Table 1). Although there are variations in maximum elevation, the range of elevations is constant over time (after the 50 Myr periods of initialization, which are not shown here). These data show that all simulations assessed in scenario 4 had achieved a dynamic equilibrium such that the range of elevations was constant with time. Larger variations in maximum elevation occur for larger contrasts in erodibility.

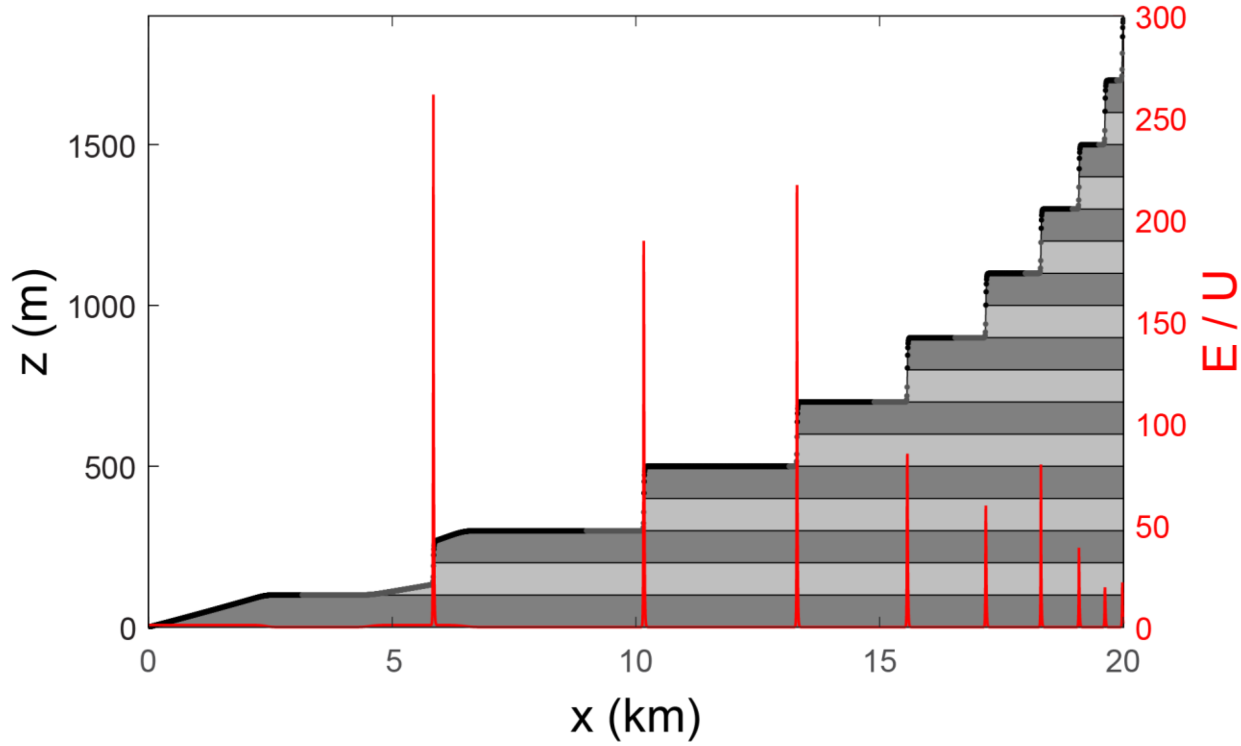

Figure S5. Longitudinal profile for a simulation using $n = 1$. Here, the strong layer (dark gray) has erodibility $K_S = 5\times10^{-7}$ a^{-1}, while the weak layer (light gray) has $K_W = 10^{-6}$ a^{-1}. Here, the rock-uplift rate U is 0.15 mm a^{-1}, and the layer thickness H is 100 m. At a distance upstream of the outlet sufficient to obscure the influence of base-level effects, the stream's slopes are either zero or infinite (zero in the flat reaches, infinite at the steps).

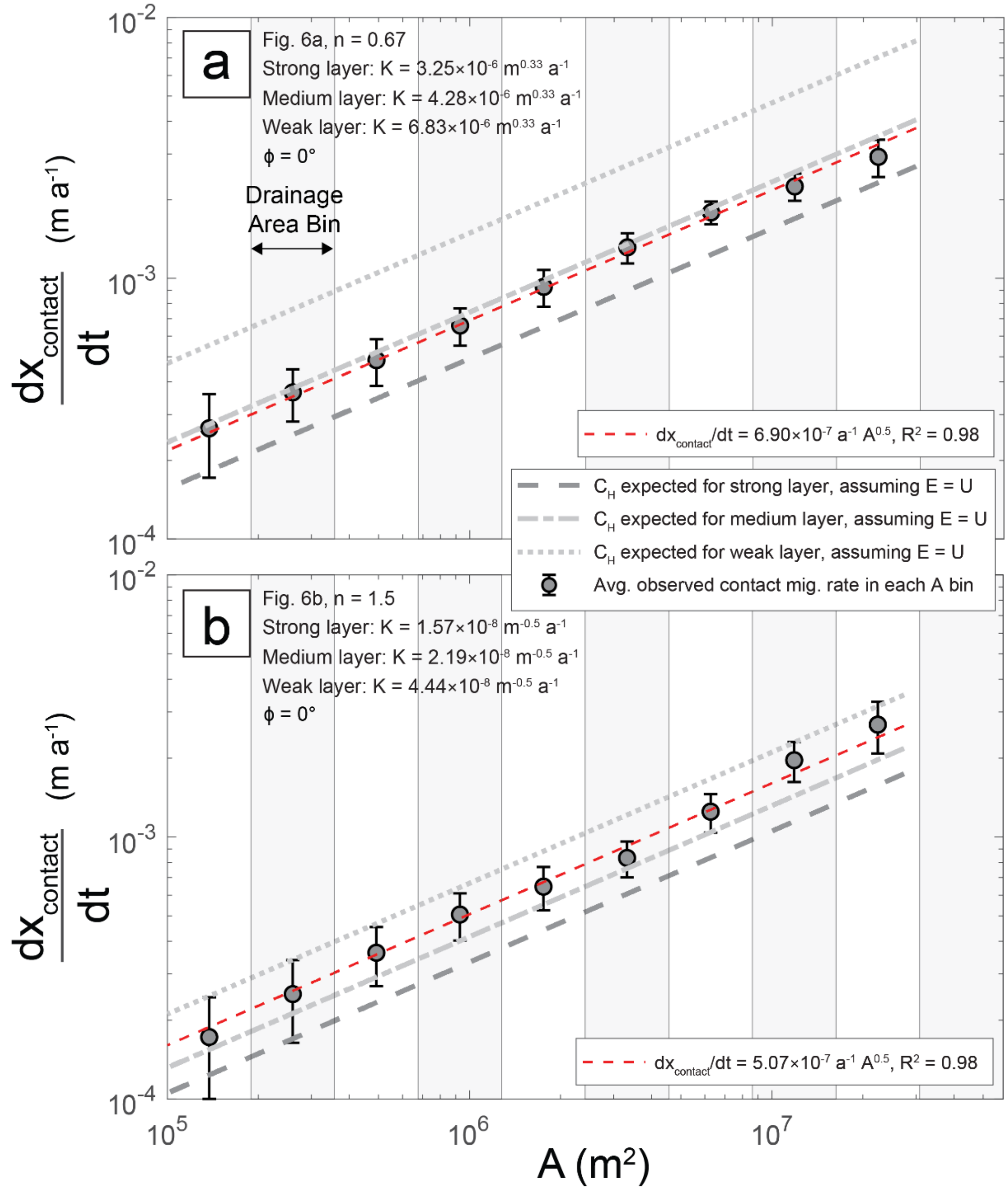

Figure S6. (**a**) Contact migration rates ($dx_{contact} / dt$) vs drainage area (A) for the simulation shown in Fig. 6a. (**b**) Contact migration rates vs drainage area for the simulation shown in Fig. 6b. The slope exponent (n) and weak, medium, and strong erodibilities (K_W, K_M, and K_S) are shown in the upper left of each subplot. Note that contact dip (ϕ) here is 0°. Each subplot has dotted, dash-dot, and dashed lines for the kinematic wave speeds estimated for the weak, medium, and and strong layers, respectively, if the erosion rate (E) was equal to rock-uplift rate (U). The erosion rates in each layer do not conform to this assumption, however, and instead vary so that kinematic wave speed is maintained at a moderate value between these different lines.

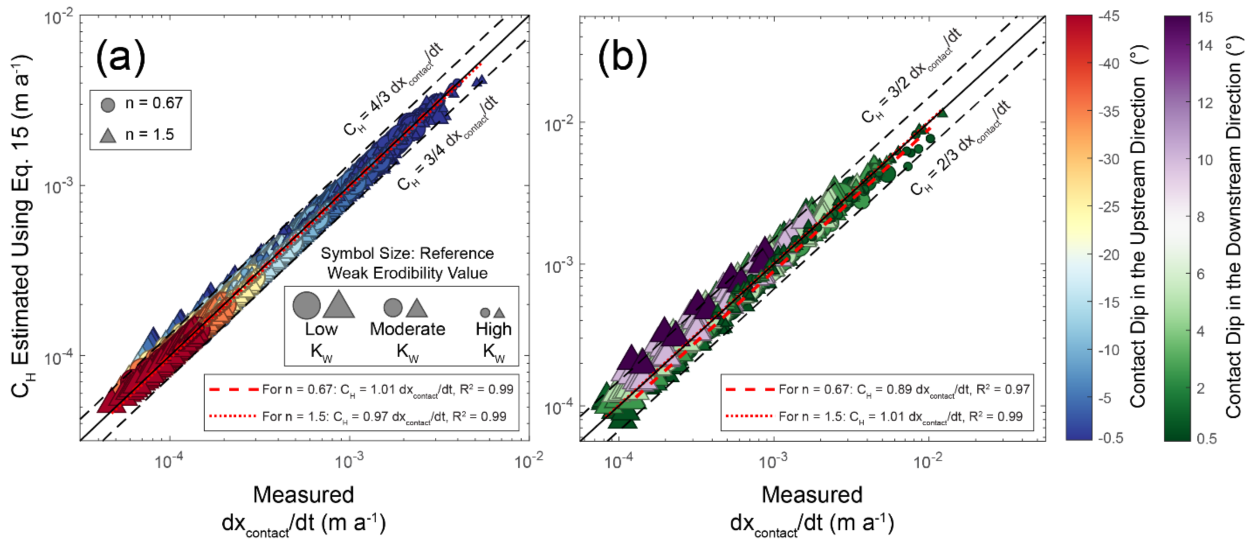

Figure S7. Contact migration rates measured in our models ($dx_{contact}/dt$) vs. kinematic wave speeds (C_H) estimated using Eq. 15. Note that this is a version of Fig. 10 that uses all k_{sn} measured over the 10 Myr duration for each simulation (instead of only the final model timestep). Subplot (**a**) shows results for scenario 3 (contacts dipping upstream, $\phi < 0°$) and subplot (**c**) shows results for scenario 4 (contacts dipping downstream, $\phi > 0°$). Red dashed and dotted lines are linear regressions for results with n values of 0.67 and 1.5, respectively. Dashed lines show the minimum and maximum values for most values in each subplot, with labels denoting the corresponding relationships between observed contact migration rate and estimated kinematic wave speed.

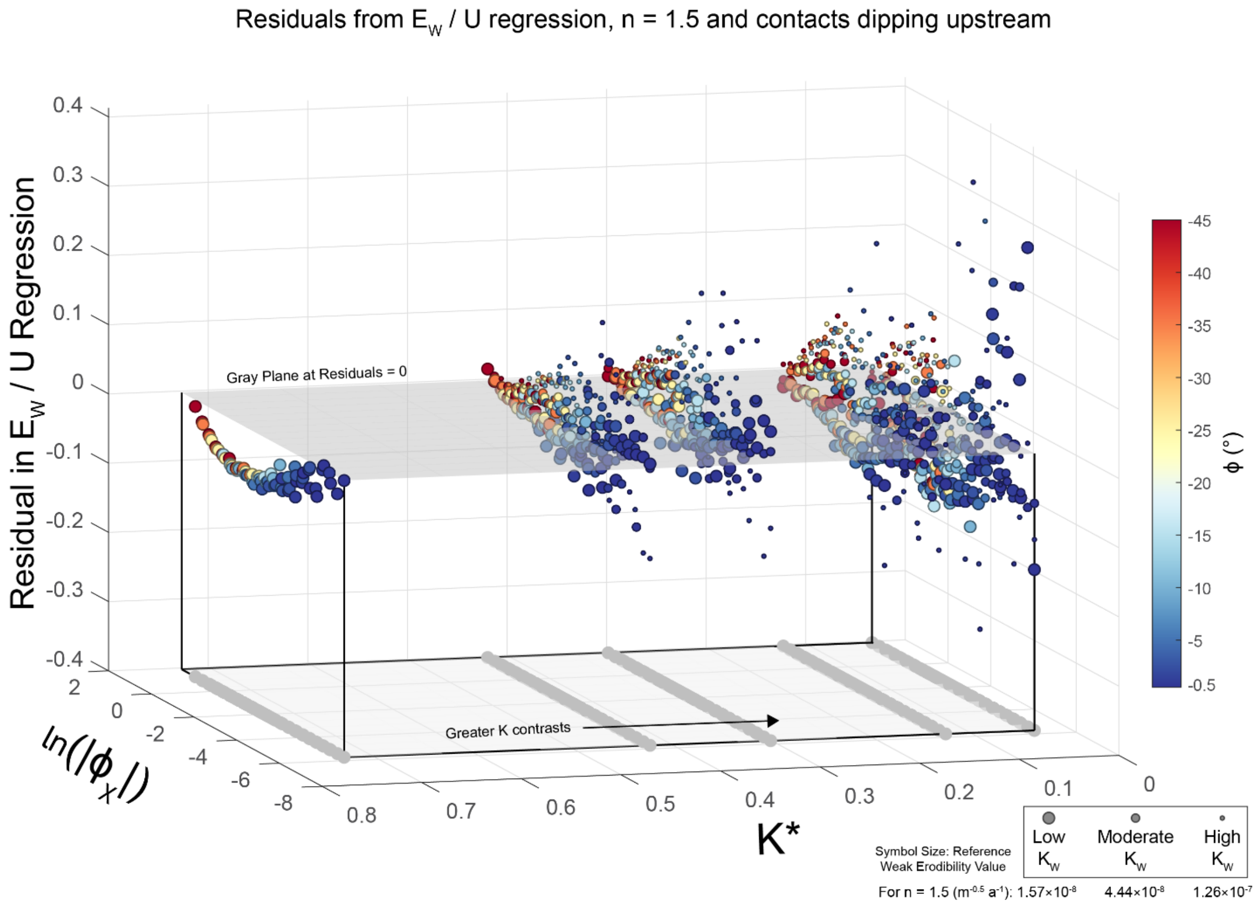

Figure S8. Residuals for the three-dimensional regression of E_W / U shown in Fig. 11 (n = 1.5, contacts dipping upstream).

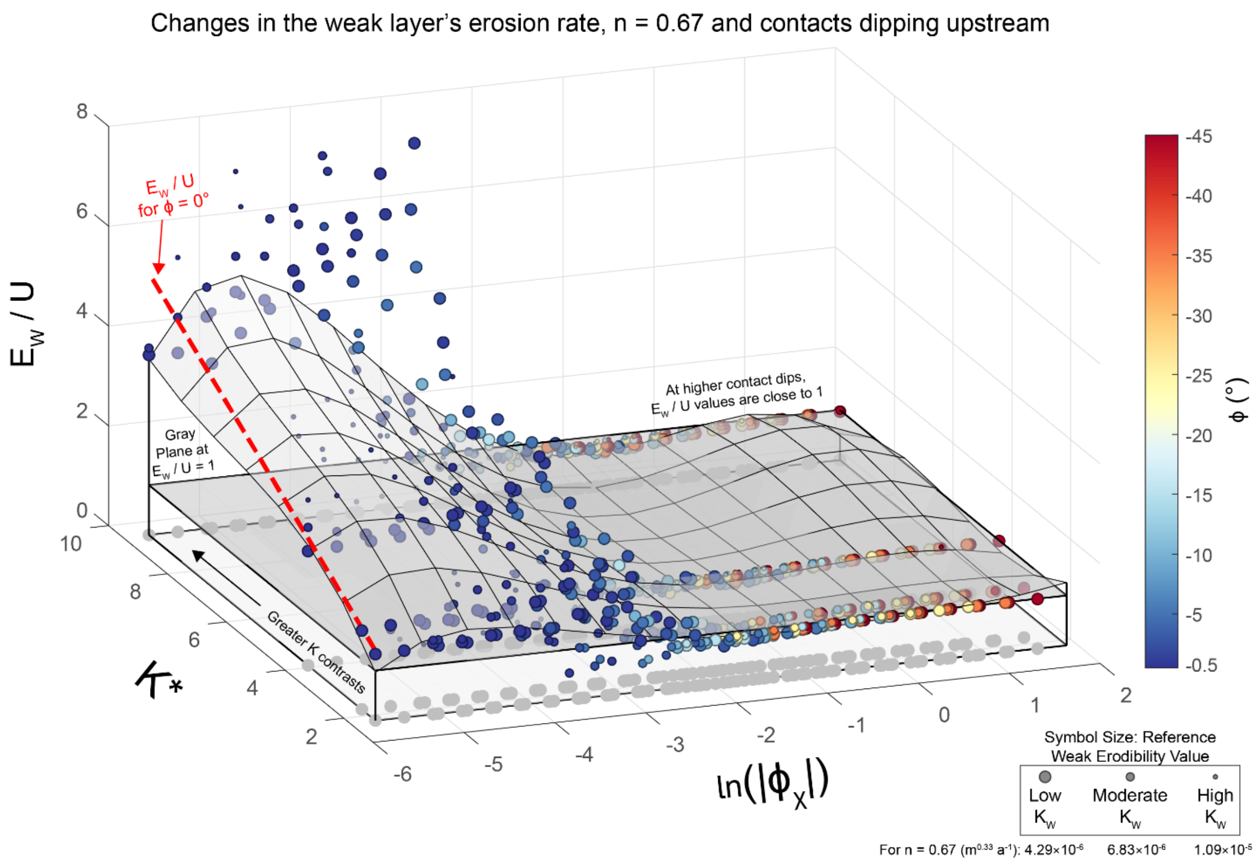

Figure S9. Variations in the average erosion rate in the weak layer (E_W) normalized by rock-uplift rate (U) with both the logarithm of the absolute contact dip in χ-space ($\log(|\phi_\chi|)$) and the enforced K^* (Eq. 9c) for simulations with n = 0.67 and contacts dipping upstream ($\phi < 0°$). Note that points are colored by ϕ and have shadows directly beneath them. A gray plane is situated at E_W / U values of one to highlight that points at high $\log(|\phi_\chi|)$ values (> -2) generally have E_W / U values of about one. A regression is fit to all data ($R^2 = 0.64$): $E_W / U = (1.4\times10^{-3} \ln(|\phi_\chi|)^5) + (-2.9\times10^{-3} \ln(|\phi_\chi|)^4 K^*) + (1.3\times10^{-2} \ln(|\phi_\chi|)^4) + (9.7\times10^{-4} \ln(|\phi_\chi|)^3 K^{*2}) + (-3.0\times10^{-2} \ln(|\phi_\chi|)^3 K^*) + (4.8\times10^{-2} \ln(|\phi_\chi|)^3) + (-6.1\times10^{-4} \ln(|\phi_\chi|)^2 K^{*3}) + (1.3\times10^{-2} \ln(|\phi_\chi|)^2 K^{*2}) + (-8.2\times10^{-2} \ln(|\phi_\chi|)^2 K^*) + (1.2\times10^{-1} \ln(|\phi_\chi|)^2) + (-5.9\times10^{-3} \ln(|\phi_\chi|) K^{*3}) + (9.1\times10^{-2} \ln(|\phi_\chi|) K^{*2}) + (-3.4\times10^{-1} \ln(|\phi_\chi|) K^*) + (4.3\times10^{-1} \ln(|\phi_\chi|)) + (-2.4\times10^{-3} K^{*3}) + (3.5\times10^{-2} K^{*2}) + (-1.4\times10^{-1} K^*) + 1.1\times10^0$. Note that points are colored by ϕ and have shadows directly beneath them. The red dashed line represents the erosion rates expected if the contact dip was 0° (Eqs. 8 and 12).

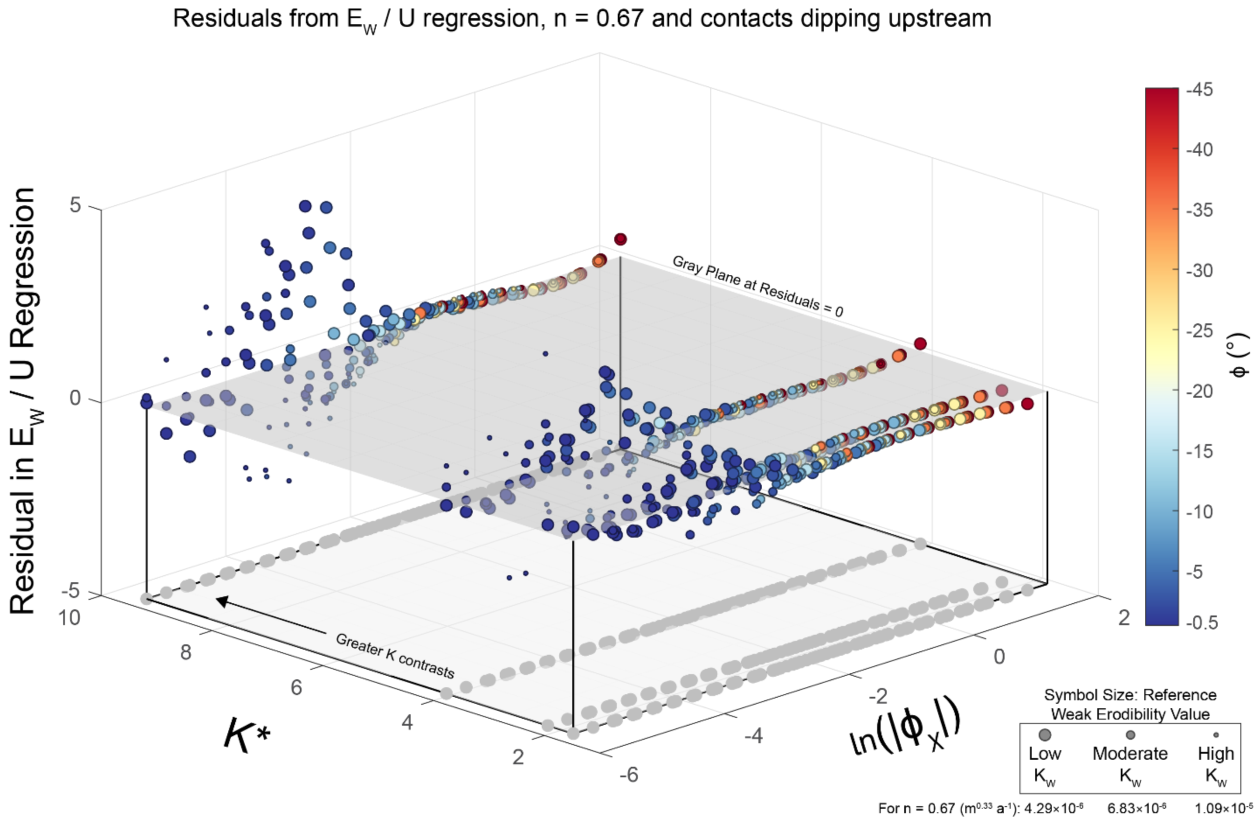

Figure S10. Residuals for the three-dimensional regression of E_W / U shown in Fig. S9 (n = 0.67, contacts dipping upstream).

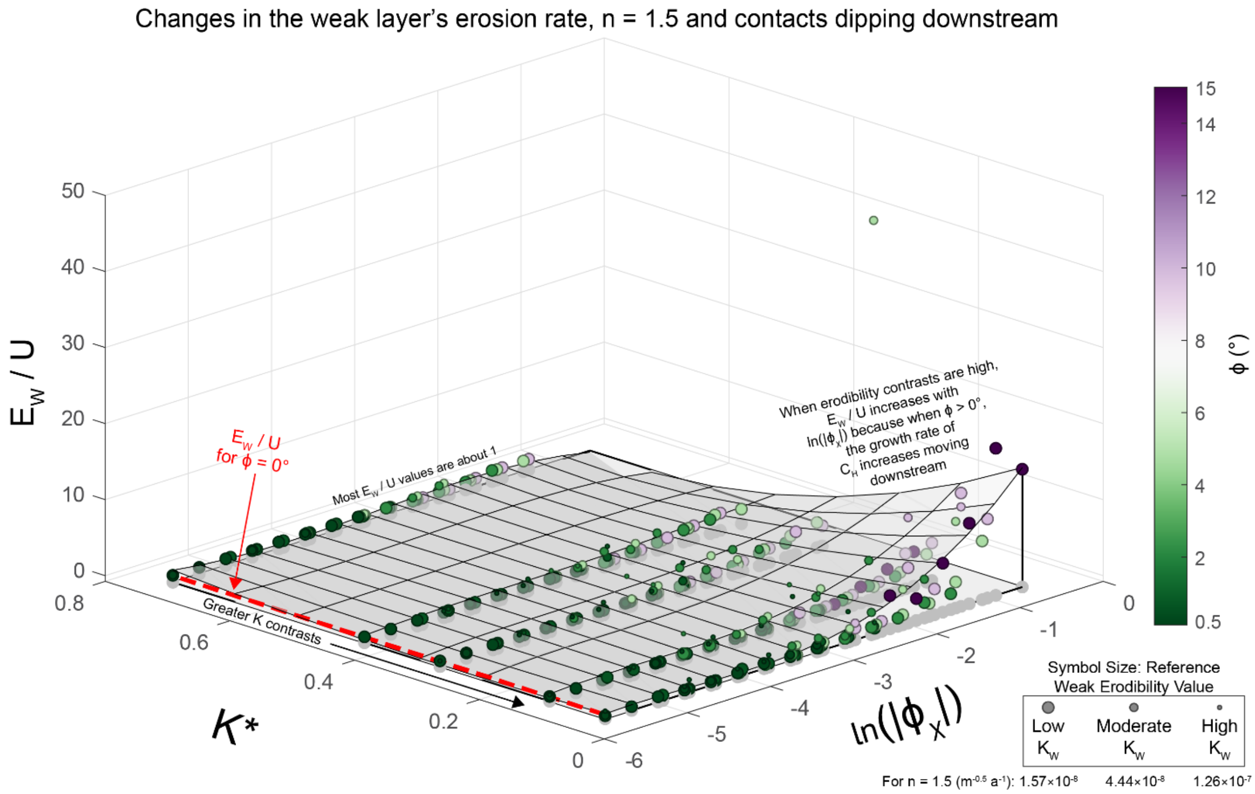

Figure S11. Variations in the average erosion rate in the weak layer (E_W) normalized by rock-uplift rate (U) with both the logarithm of the absolute contact dip in χ-space (log(|ϕ_χ|)) and the enforced K^* (Eq. 6) for simulations with n = 1.5 and contacts dipping downstream ($\phi > 0°$). A regression is fit to all data (R^2 = 0.32): $E_W / U = (-6.0\times10^{-3} \ln(|\phi_\chi|)^4) + (-5.6\times10^{-1} \ln(|\phi_\chi|)^3 K^*) + (1.9\times10^{-1} \ln(|\phi_\chi|)^3) + (3.7\times10^{0} \ln(|\phi_\chi|)^2 K^{*2}) + (-9.9\times10^{0} \ln(|\phi_\chi|)^2 K^*) + (3.6\times10^{0} \ln(|\phi_\chi|)^2) + (3.0\times10^{1} \ln(|\phi_\chi|) K^{*2}) + (5.9\times10^{1} K^{*2}) + (-5.3\times10^{1} \ln(|\phi_\chi|) K^*) + (1.8\times10^{1} \ln(|\phi_\chi|)) + (-8.6\times10^{1} K^*) + 2.8\times10^{1}$. Note that points are colored by ϕ and have shadows directly beneath them. The red dashed line represents the erosion rates expected if the contact dip was 0° (Eq. 12).

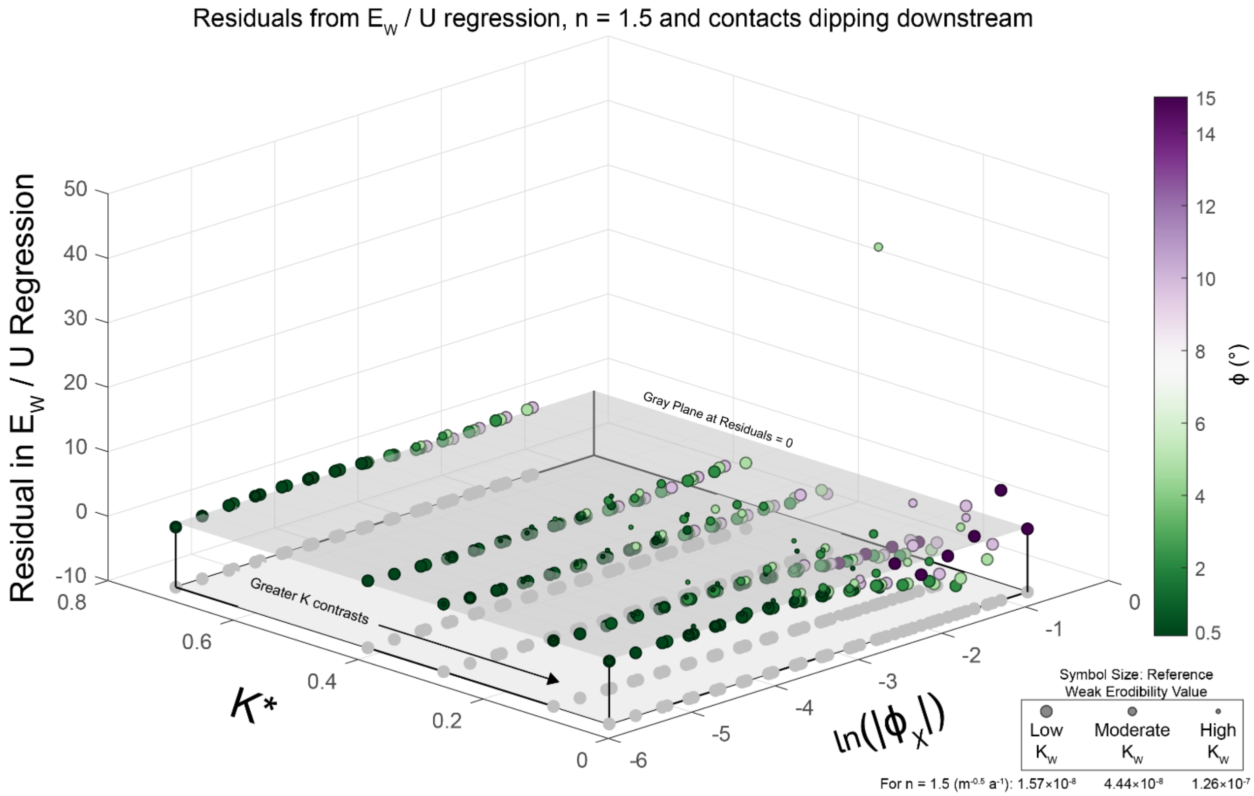

Figure S12. Residuals for the three-dimensional regression of E_W / U shown in Fig. S11 (n = 1.5, contacts dipping downstream).

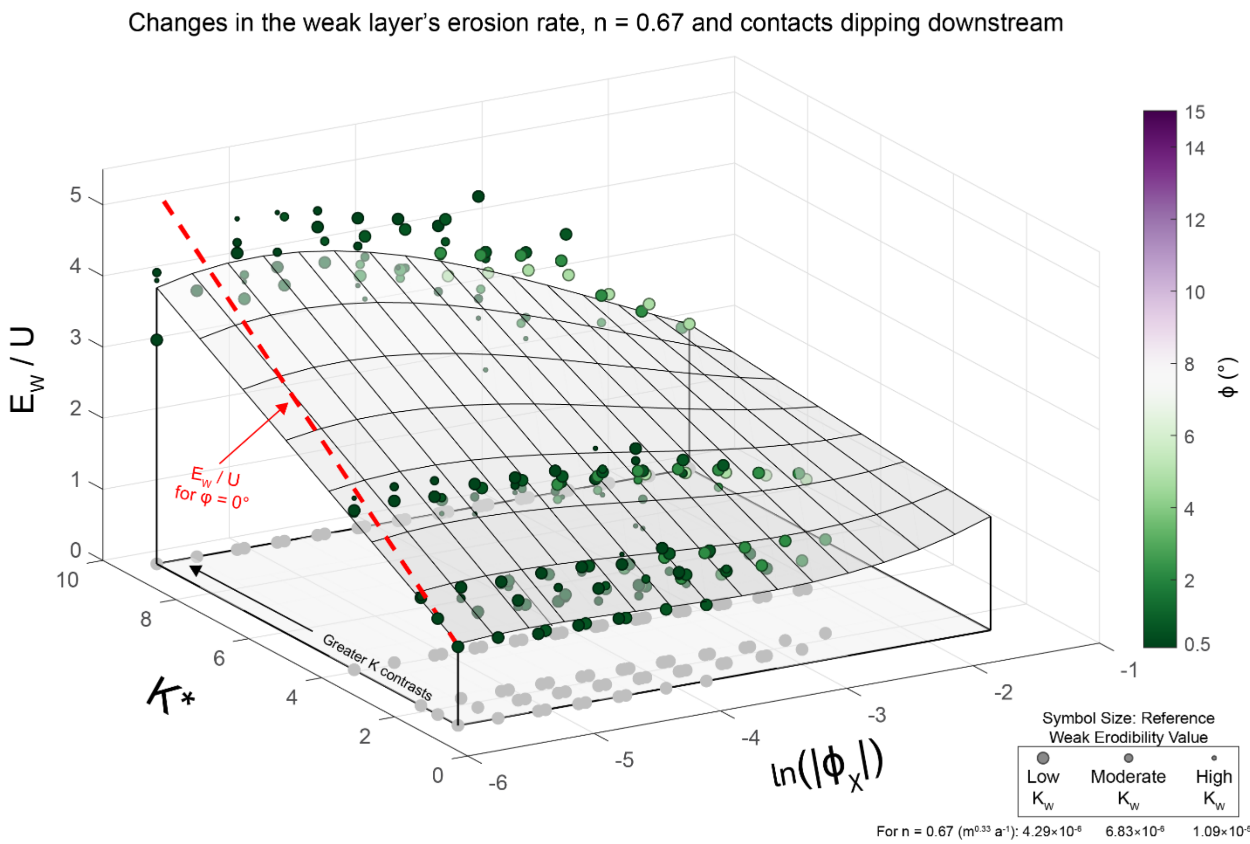

Figure S13. Variations in the average erosion rate in the weak layer (E_W) normalized by rock-uplift rate (U) with both the logarithm of the absolute contact dip in χ-space ($\log(|\phi_\chi|)$) and the enforced K^* (Eq. 9c) for simulations with $n = 0.67$ and contacts dipping downstream ($\phi > 0°$). A regression is fit to all data ($R^2 = 0.92$): $E_W / U = (3.3\times10^{-2} \ln(|\phi_\chi|)^3) + (-2.6\times10^{-2} \ln(|\phi_\chi|)^2 K^*) + (4.5\times10^{-1} \ln(|\phi_\chi|)^2) + (-2.5\times10^{-1} \ln(|\phi_\chi|) K^*) + (2.0\times10^0 \ln(|\phi_\chi|)) + (-2.7\times10^{-1} K^*) + 3.6\times10^0$. Note that points are colored by ϕ and have shadows directly beneath them. The red dashed line represents the erosion rates expected if the contact dip was 0°.

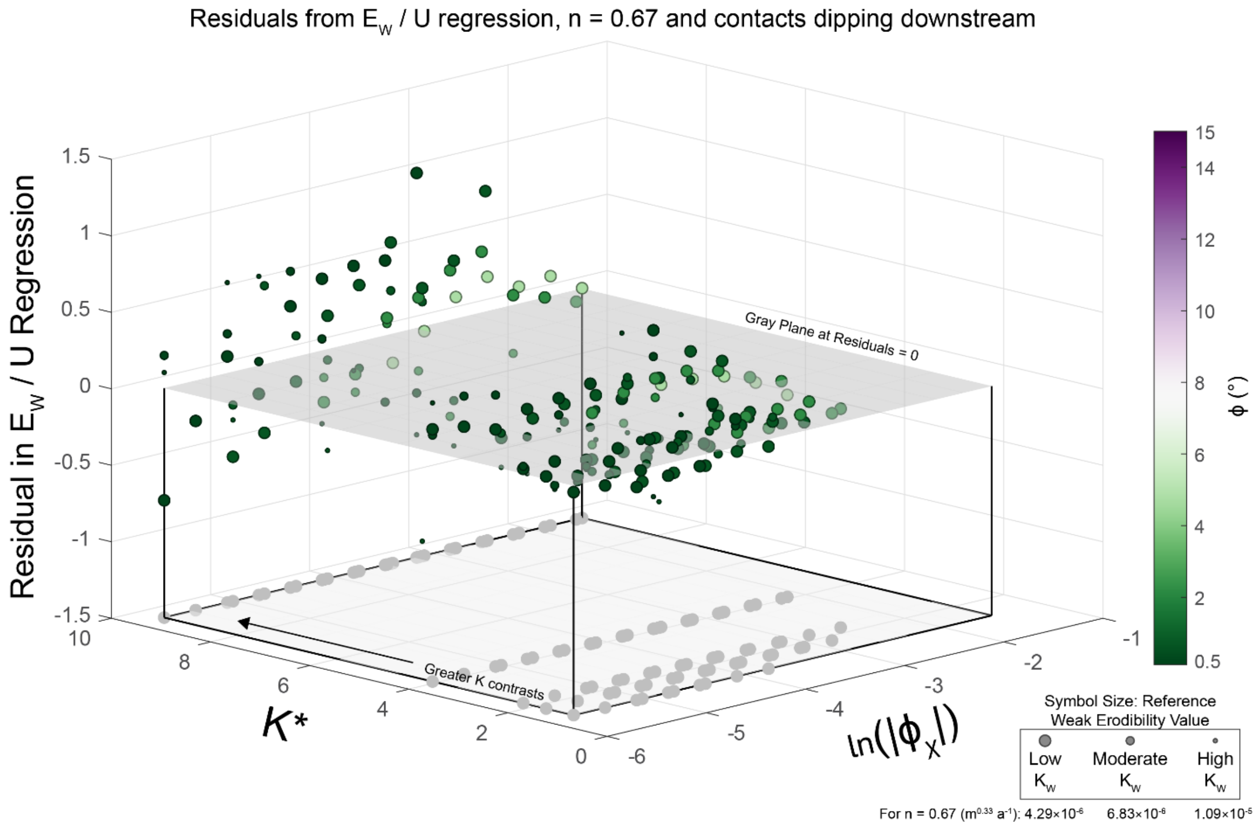

Figure S14. Residuals for the three-dimensional regression of E_W / U shown in Fig. S13 (n = 0.67, contacts dipping downstream).

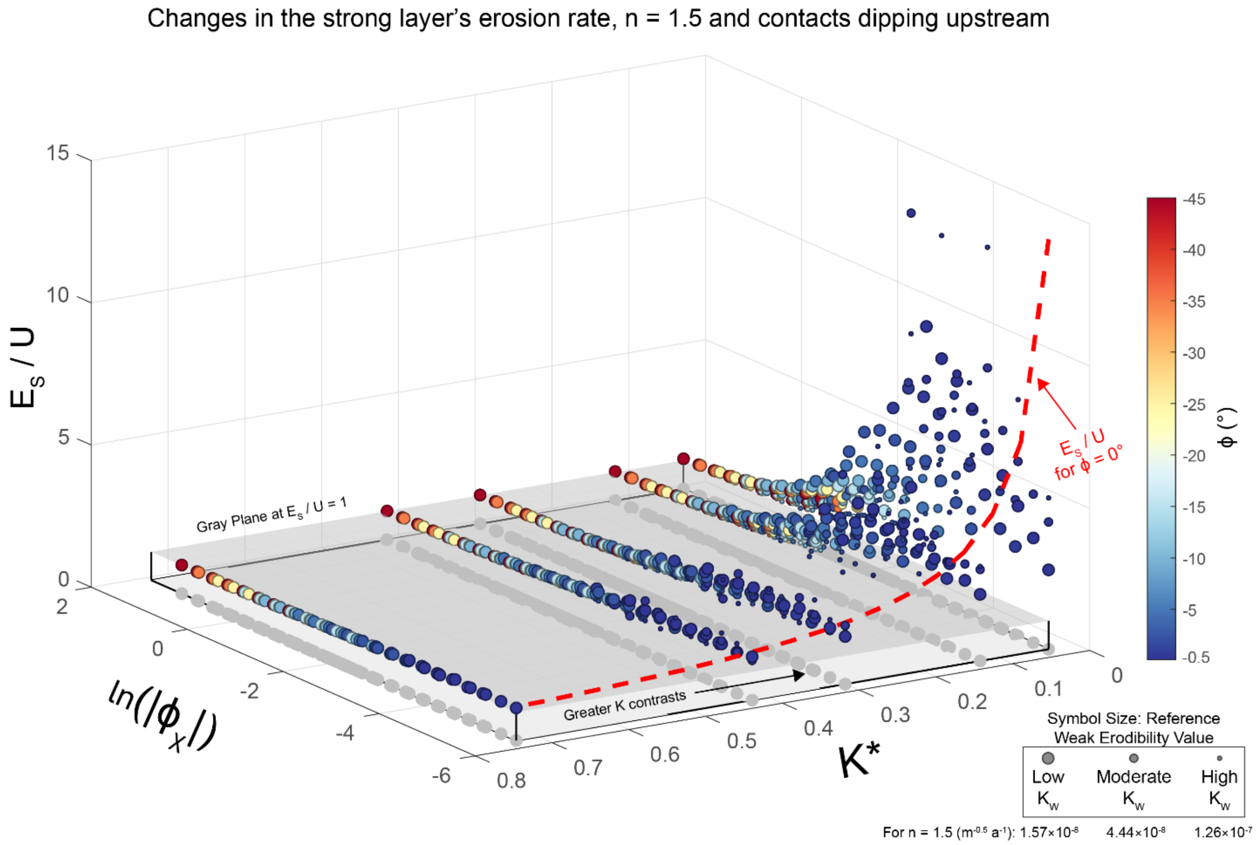

Figure S15. Variations in the average erosion rate in the strong layer (E_S) normalized by rock-uplift rate (U) with both the logarithm of the absolute contact dip in χ-space ($\ln(|\phi_\chi|)$) and the enforced K^* (Eq. 9c) for simulations with $n = 1.5$ and contacts dipping upstream ($\phi < 0$º). Note that symbol size represents the reference weak erodibility (K_W), with smaller points corresponding with higher K_W values. Also note that the E_S / U and $\ln(|\phi_\chi|)$ values here are the mean values taken within logarithmically spaced drainage area bins (e.g., Fig. 9). Points are colored by ϕ and have shadows directly beneath them. The red dashed line represents the erosion rates expected if the contact dip was 0° (Eq. 12). A gray plane is situated at E_S / U values of one.

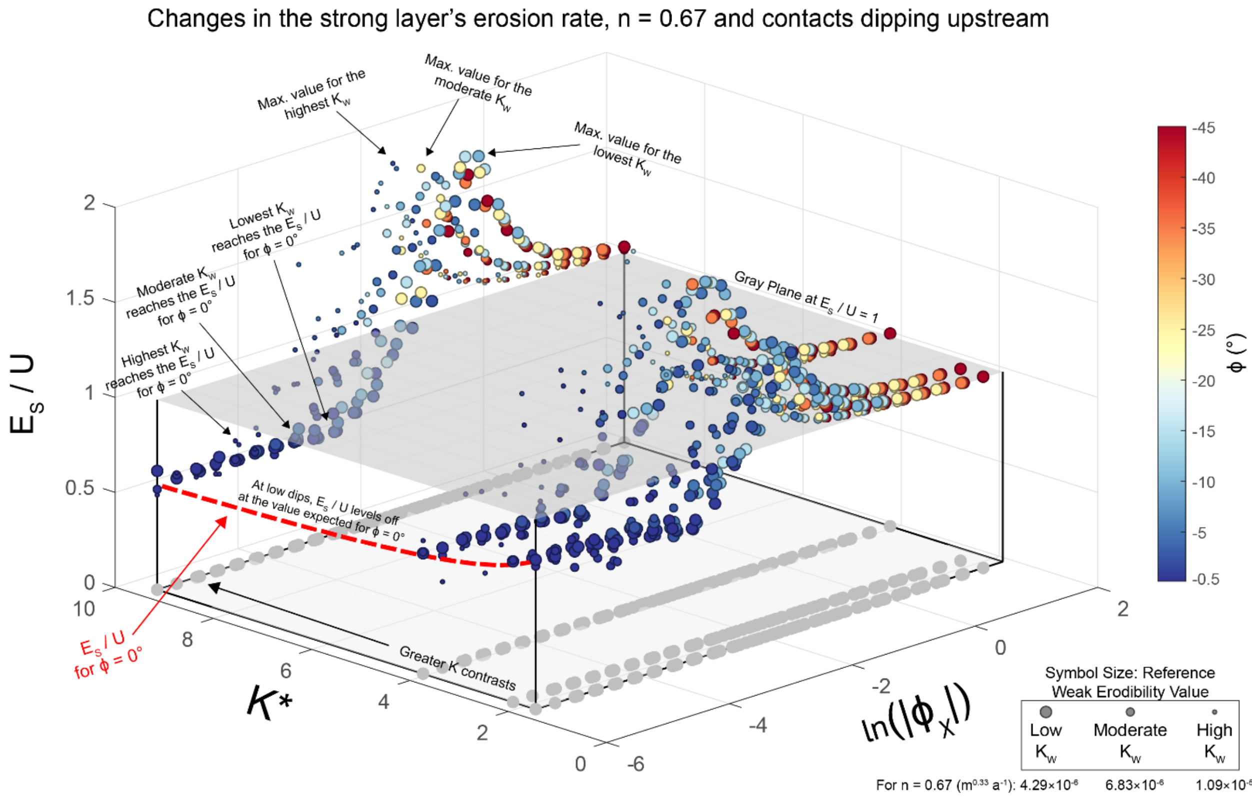

Figure S16. Variations in the average erosion rate in the strong layer (E_S) normalized by rock-uplift rate (U) with both the logarithm of the absolute contact dip in χ-space ($\log(|\phi_\chi|)$) and the enforced K^* (Eq. 9c) for simulations with $n = 0.67$ and contacts dipping upstream ($\phi < 0°$). Note that points are colored by ϕ and have shadows directly beneath them. The red dashed line represents the erosion rates expected if the contact dip was 0° (Eq. 12). The positions of maximum and minimum E_S / U values change with the reference weak erodibility (K_W).

Explanation of Figure S16:

The complex patterns in Fig. S16 occur because stretch zones (Royden and Perron, 2013) form when $n < 1$ and contacts dip upstream. A stretch zone is a gap between slope patches; an example of a stretch zone that many would recognize is the broad, convex-upwards knickzone that sometimes occurs along transient bedrock rivers. Gaps between slope patches occur when $n < 1$ because the slope patches for higher rates of base level fall ("high-*E*" slope patches) migrate upstream at a slower rate than the slope patches for lower rates of base level fall ("low-*E*" slope patches). Higher erosion rates within a weak unit can undercut the strong unit, generating high-E slope patches and a stretch zone. Examples of these dynamics are in Fig. 7c. Near the basin outlet, the strong unit has a high steepness and the weak unit has a low steepness. Moving upstream, a steep reach begins to form at the top of each reach within the weak unit, and reaches within the strong unit have a curved, convex-upwards morphology. These convex reaches are the stretch zones. Moving further upstream, eventually each reach within the weak unit has a high steepness, while each reach within the strong has a low steepness (approaching the behavior for a contact dip of 0°). These longitudinal changes in stream morphology are the physical representation of the trends in Fig. S16; the maximum erosion rates in Fig. S16 (E_S / U) occur right before the reaches within the strong unit begin to be dominated by convex stretch zones. The erosion rates decrease with $\ln(|\phi_\chi|)$ past this point because the influence of contact migration becomes less significant at higher contact dips.

The reason the positions of maximum and minimum erosion rates change with the reference weak erodibility (K_W) in Fig. S16 is because erodibility influences the turning point at which stretch zones begin to dominate each reach within the strong unit (also the point at which the weak unit begins to have a pronounced section with high steepness).

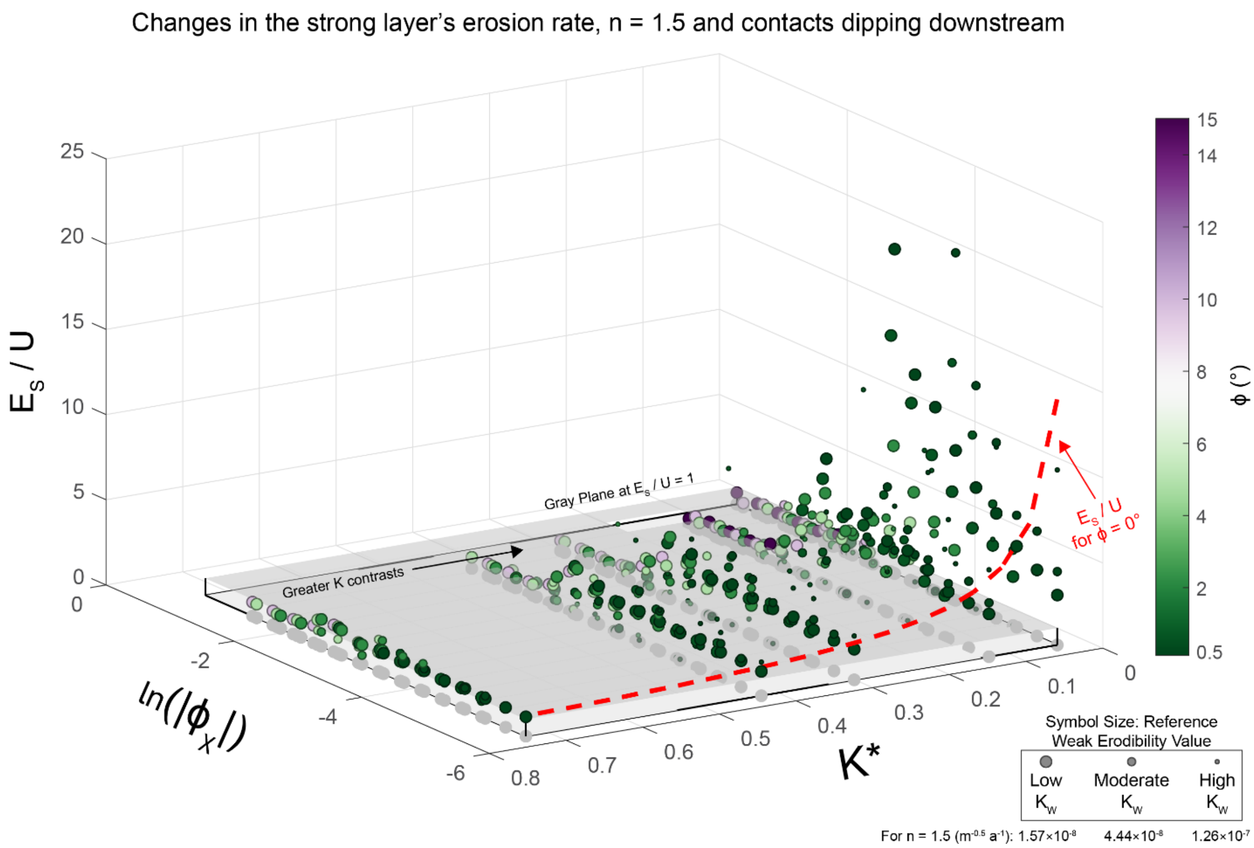

Figure S17. Variations in the average erosion rate in the strong layer (E_S) normalized by rock-uplift rate (U) with both the logarithm of the absolute contact dip in χ-space ($\ln(|\phi_\chi|)$) and the enforced K^* (Eq. 9c) for simulations with n = 1.5 and contacts dipping downstream ($\phi > 0$º). Note that symbol size represents the reference weak erodibility (K_W), with smaller points corresponding with higher K_W values. Also note that the E_S / U and $\ln(|\phi_\chi|)$ values here are the mean values taken within logarithmically spaced drainage area bins (e.g., Fig. 9). Points are colored by ϕ and have shadows directly beneath them. The red dashed line represents the erosion rates expected if the contact dip was 0° (Eq. 12). A gray plane is situated at E_S / U values of one.

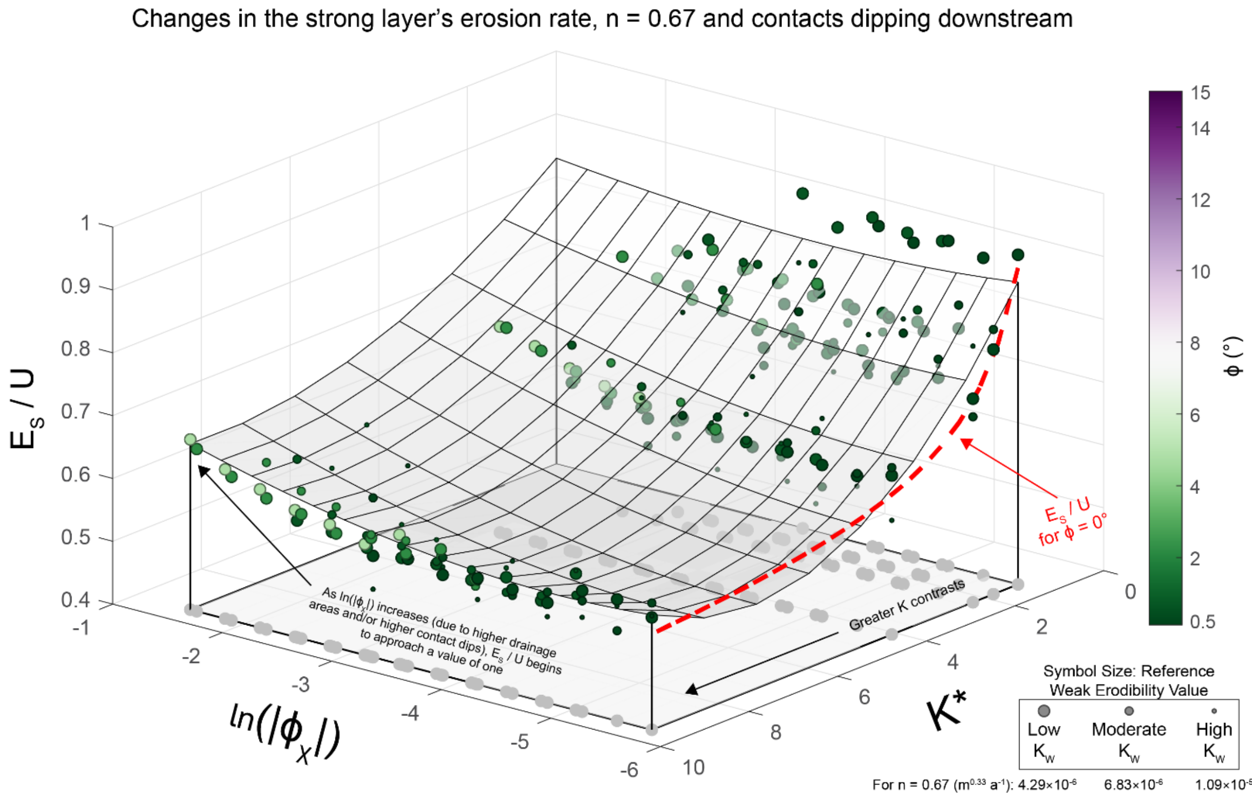

Figure S18. Variations in the average erosion rate in the strong layer (E_S) normalized by rock-uplift rate (U) with both the logarithm of the absolute contact dip in χ-space ($\ln(|\phi_\chi|)$) and the enforced K^* (Eq. 9c) for simulations with $n = 0.67$ and contacts dipping downstream ($\phi > 0^{\circ}$). Note that symbol size represents the reference weak erodibility (K_W), with smaller points corresponding with higher K_W values. Also note that the E_S / U and $\ln(|\phi_\chi|)$ values here are the mean values taken within logarithmically spaced drainage area bins (e.g., Fig. 9). Points are colored by ϕ and have shadows directly beneath them. The red dashed line represents the erosion rates expected if the contact dip was 0° (Eq. 12). A regression is fit to all data ($R^2 = 0.91$): $E_S / U = (-3.7\times10^{-4} \ln(|\phi_\chi|)^3) + (3.4\times10^{-4} \ln(|\phi_\chi|)^2 K^*) + (7.1\times10^{-4} \ln(|\phi_\chi|)^2) + (-1.4\times10^{-3} \ln(|\phi_\chi|) K^{*2}) + (1.9\times10^{-2} \ln(|\phi_\chi|) K^*) + (3.7\times10^{-3} \ln(|\phi_\chi|)) + (1.8\times10^{-3} K^{*2}) + (-4.0\times10^{-2} K^*) + 9.7\times10^{-1}$.

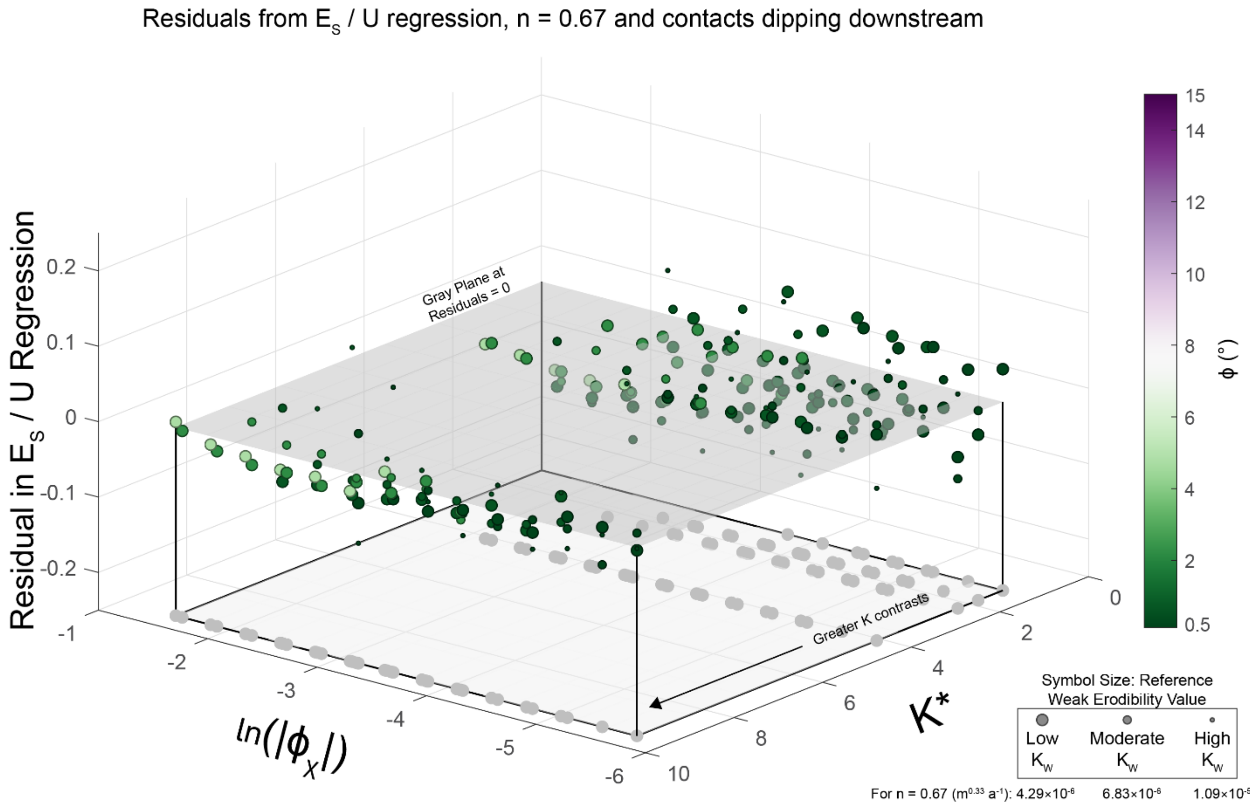

Figure S19. Residuals for the three-dimensional regression of E_S / U shown in Fig. S18 (n = 0.67, contacts dipping downstream).

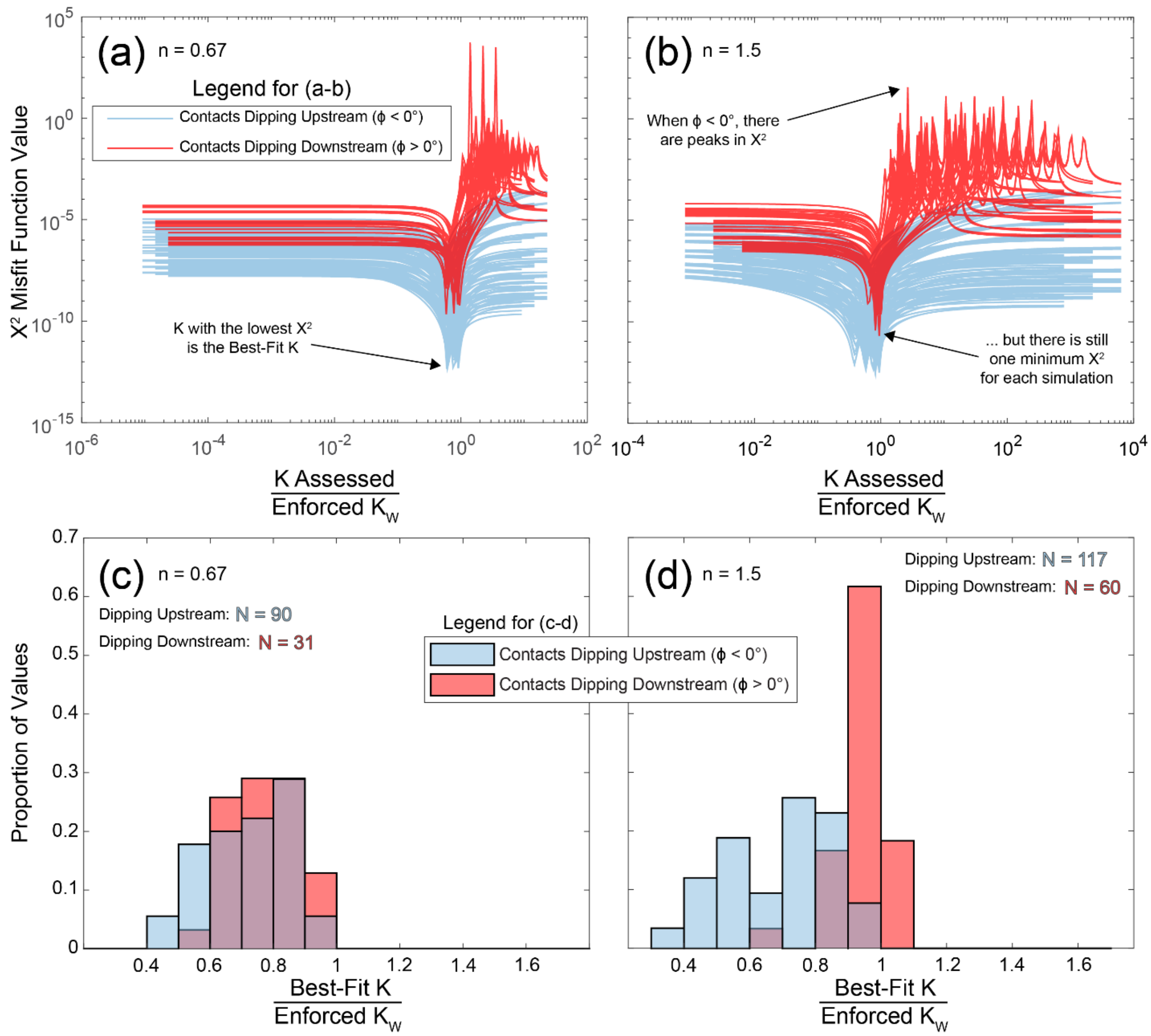

Figure S20. Comparison of best-fit K values in our numerical models to the weak erodibility (K_W) used in each simulation. Note that this is a version of Fig. 12 where we calculate Eq. 15 estimates of kinematic wave speed using all k_{sn} values recorded over the entire 10 Myr duration for each simulation (rather than only the final timestep). (**a-b**) X^2 Misfit Function values for kinematic wave speeds (C_H) estimated using Eq. 14, the enforced contact dip (ϕ), and a wide range of K values (200 points spaced logarithmically from 10^{-9} to 10^{-4} $m^{1-2n\theta} a^{-1}$, where $\theta = 0.5$) relative to the Eq. 15 estimates of C_H. (**c-d**) Comparison between the best-fit K and the K_W enforced in the simulations. Subplots (**a**) and (**c**) show results for n = 0.67, while subplots (**b**) and (**d**) show results for n = 1.5.

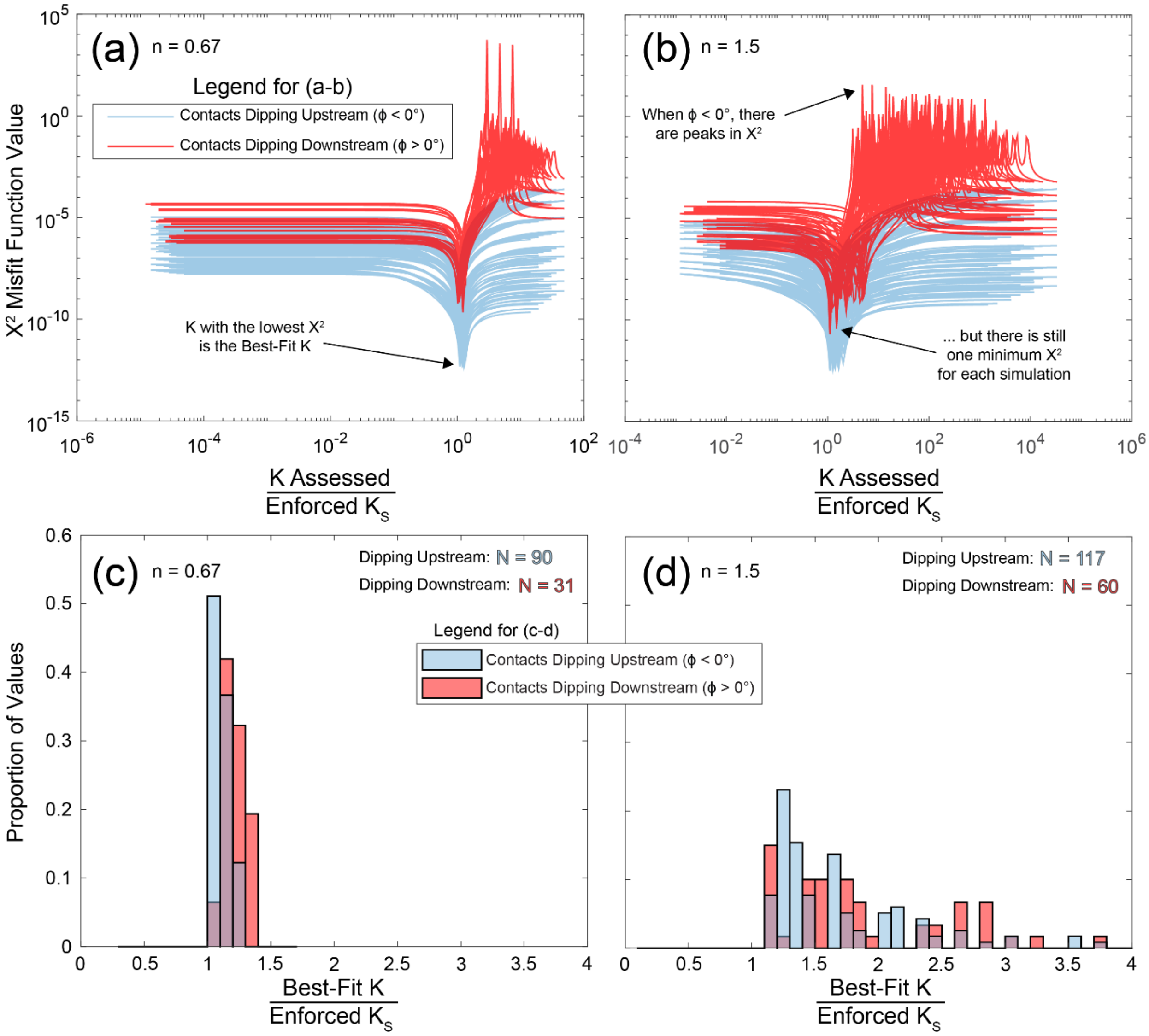

Figure S21. Comparison of best-fit K values in our numerical models to the strong erodibility (K_S) used in each simulation. Note that this is a version of Fig. 13 where we calculate Eq. 15 estimates of kinematic wave speed using all k_{sn} values recorded over the entire 10 Myr duration for each simulation (rather than only the final timestep). (**a-b**) X^2 Misfit Function values for kinematic wave speeds (C_H) estimated using Eq. 14, the enforced contact dip (ϕ), and a wide range of K values (200 points spaced logarithmically from 10^{-9} to 10^{-4} $m^{1-2n\theta} a^{-1}$, where $\theta = 0.5$) relative to the Eq. 15 estimates of C_H. (**c-d**) Comparison between the best-fit K and the K_S enforced in the simulations. Subplots (**a**) and (**c**) show results for n = 0.67, while subplots (**b**) and (**d**) show results for n = 1.5.